Received: 12 January 2018 | Accepted: 3 February 2018
DOI: 10.1002/maco.201810049

ARTICLE

Materials and Corrosion

Effect of HAP decomposition on the corrosion behavior of Ti–HAP biocomposites

Fatih Toptan[1,2] | Alexandra C. Alves[1] | Margarida A. Ferreira[1] | Catarina I. da Silva Oliveira[1] | Ana M.P. Pinto[1,2]

[1] CMEMS-UMinho, Center for MicroElectroMechanical Systems, Universidade do Minho, Azurém, 4800-058 Guimarães, Portugal

[2] Departamento de Engenharia Mecânica, Universidade do Minho, Azurém, 4800-058 Guimarães, Portugal

Correspondence
Fatih Toptan, CMEMS-UMinho, Center for MicroElectroMechanical Systems, Universidade do Minho, Azurém, 4800-058 Guimarães, Portugal.
Email: ftoptan@dem.uminho.pt

Funding information
Fundação para a Ciência e a Tecnologia, Grant numbers: EXCL/SEM-TEC/0460/2012, M-ERA-NET/0001/2015, UID/EEA/04436/2013; European Regional Development Fund, Grant number: POCI-01-0145-FEDER-006941

Ti–HAP biocomposites are gained attention for combining the attractive properties of Ti and hydroxyapatite (HAP). However, the decomposition of HAP at elevated processing temperatures is a major concern since it can lead to structural flaws and may deteriorate the corrosion resistance of Ti. The present study aims to investigate the corrosion behavior of Ti–HAP composite processed by powder metallurgy by performing potentiodynamic polarization and electrochemical impedance spectroscopy in 0.9 wt% NaCl solution at body temperature. Results show that the presence of Ti lowers the HAP decomposition temperatures resulting in the formation of HAP-depleted zones acting as electrochemically active sites, decreasing the corrosion resistance.

KEYWORDS
corrosion, hydroxyapatite, powder metallurgy, titanium

1 | INTRODUCTION

Owing to its similar chemical and crystallographic structure to the bone mineral, hydroxyapatite (HAP) has a strong chemical bonding ability to bone. However, its poor mechanical properties limit the use of HAP on load-bearing implants. As contrary, Ti and its alloys have good mechanical properties, in addition to their excellent electrochemical properties, however, its bio-inertness is a clinical concern.[1–4] Traditionally, HAP was used as a coating material applied on Ti substrates by various techniques for enhanced bioactivity. However, failure at the metal–coating interface, consequent formation of HAP debris, and their possible contribution to wear of the implant as third-body particles are some major concerns.[5,6]

Ti–HAP biocomposites are considered as an alternative solution to combine the attractive properties of Ti and HAP.[3,6–8] Several studies are available in the literature investigating these biocomposites in the form of homogenous composites,[3,6,7,9–17] functionally graded materials (FGM),[18–21] and homogenous or graded composite coatings.[2,4,22–31] Within these studies, powder metallurgy (P/M) was the most popular route to process bulk composites, whereas plasma spraying and sputtering were the most popular routes to process composite coatings. However, one of the major concern within all the processes requiring elevated temperatures is the stability of the HAP during processing.[10]

It has been reported that transformations occur in HAP at elevated temperatures through two stages including expulsion of water yielding the formation of oxyapatite followed by its decomposition resulting in the formation of calcium phosphates.[32–34] Various decomposition temperatures

were reported in the literature, which have been stated to be affected by several factors including the purity of HAP, atmosphere or water vapor pressure.[32,33,35]

Several researchers reported that dehydroxylation and decomposition of HAP are accelerated in the presence of Ti, and it can be started at temperatures as low as 800 °C.[8,10,21,35,36] Weng et al.[36] sintered Ti–HAP composites in vacuum and reported that Ti catalyzed the thermal decomposition of HAP, where HAP started to decompose at 800 °C with the formation of α-tricalcium phosphate ($Ca_3(PO_4)_2$), and tetracalcium phosphate ($Ca_4P_2O_9$). As the temperature increased, these processes were intensified but no other phases were reported. Yang et al.[37] also studied the interaction between Ti and HAP at 1100 °C in vacuum, on the compacted powders containing 80 and 90 wt% HAP and reported the formation of the decomposition products of α-tricalcium phosphate, tetracalcium phosphate, and calcium titanium oxide ($Ca_2Ti_2O_5$), where no metallic Ti was observed after processing. Ye et al.[10] processed pure HAP and Ti–50 wt% HAP composites by sintering under argon atmosphere at temperatures between 800 and 1200 °C, and explored the decomposition behavior by using Fourier transform infrared (FTIR) spectroscopy. The authors did not observe a decomposition on the pure HAP, whereas, on the composites, decomposition of HAP was observed even at 800 °C, where the dominant decomposition products were reported as tetracalcium phosphate and calcium oxide (CaO), but the presence of calcium titanate ($CaTiO_3$) was also observed. Balbinotti et al.[14] produced Ti–5 wt% HAP composites by sintering under argon atmosphere at 1200 °C and reported that decomposition started at approximately 1026 °C resulting in the formation of the crystal phases calcium titanate, tricalcium phosphate, Ti_xP_y, along with α-Ti. Zhang et al.[7] produced Ti–(5–30 wt%) HAP composites by spark plasma sintering (SPS) and space holder technique at 1200 °C. The authors reported calcium titanate, tricalcium phosphate, and Ti_xP_y interaction phases, together with pure Ti and TiO_2. Ning and Zhou[6] processed Ti–50 vol% HAP composites by sintering under argon atmosphere at 1200 °C under 20 MPa pressure, and reported the presence of crystalline phases calcium titanate, calcium oxide (CaO), a TiP-like phase, together with α-Ti and Ti_2O, on the as-processed samples. However, the authors also stated, based on the additional experiments performed on the samples sintered at 1000 °C, that the reactions resulting in the formation of those phases also occurred at this temperature. Bovand et al.[16] produced Ti–(10 and 30 wt%) HAP composites by milling in a planetary mill and sintering at 1150 °C under argon atmosphere and reported for the as-sintered structure the crystal phases of calcium titanate, tricalcium phosphate, and Ti_5P_3, along with Ti.

Decomposition of HAP may lead to a porous structure either by the dissolution or pulling out of the brittle phases.[3,6,13] This porous structure may affect the corrosion behavior of the composites and, therefore, eventually increase the ion releasing, which is a major concern for metallic implant materials since it can result in severe health complications, as well as failure of the implant.[38–40] Therefore, this work aims to have a preliminary insight on the effect of HAP decomposition on the electrochemical behavior on Ti–HAP composites.

2 | MATERIALS AND METHODS

Angular shaped Ti particles (Grade 2, Alfa Aesar) and spherical shaped HAP particles (nanoXIM-HAp403 Moreira da Maia, Portugal) were used as raw materials. The particle size distributions obtained by a laser particle analyser (Malvern Series 2600) are given in Table 1.

Titanium and HAP powders were mixed together with PVA (0.4 vol%) in a ball mill containing alumina balls rotated at 130 rpm during 4 h in argon atmosphere. The powder blends were compacted in a zinc stearate lubricated stainless steel die under a uniaxial pressure of 350 MPa applied for 2 min. Ti and Ti–5 vol% HAP green compacts were subjected to a dilatometric analysis by applying a heating rate of 5 °C min^{-1} under high purity Ar atmosphere (Linseis, mod.4 L70-2000).

For processing, the powder blends were prepared and compacted by following the same procedure as preparing the dilatometry samples, but using a nitrided stainless steel die. Cylindrical green compacts 12 mm in diameter and 5 mm in height were pre-heated in argon atmosphere at 400 °C during 4 h for binder removal, and sintered in a horizontal tubular furnace under high vacuum ($<10^{-5}$ mbar) during 3 h with 5 °C min^{-1} heating and cooling rates. In addition to Ti–5 vol% HAP (Ti–5HAP) composites, unreinforced Ti samples were also produced by following the same route, to be used as the control group in the electrochemical tests. Based on the dilatometric study, the sintering temperatures were selected as 1100 and 1300 °C for Ti and Ti–5HAP composites, respectively.

Microstructures were characterized by using a Leica DM2500 optical microscope (OM) and a FEI Nova 200 field emission gun scanning electron microscope (FEG-SEM), equipped with EDAX-Pegasus energy dispersive X-ray spectroscopy (EDS). Phase analysis was carried out by XRD using a Bruker D8 Discover diffractometer equipped

TABLE 1 Particle size distribution

Material	*D* [v,0.1]	*D* [v,0.5]	*D* [v,0.9]
Ti	10.42	25.33	43.47
HAP	2.44	8.34	22.11

with a Cu Kα radiation source. Since it was difficult to detect the lower amounts of the interaction products by XRD on Ti–5HAP samples, Ti–50 vol% HAP composites (Ti–50HAP) were also processed under identical conditions to Ti–5HAP composites for the structural analysis. Moreover, pure HAP powders were also sintered under identical conditions to the composites for structural comparison.

Electrochemical tests were performed in a conventional three-electrode electrochemical cell (adapted from ASTM: G3-89) containing 180 ml of 0.9 wt% NaCl electrolyte, a reference electrode (saturated calomel electrode, SCE), a counter electrode (Pt electrode), and the working electrode (samples having an exposed area of 0.38 cm^2). The electrochemical cell was placed in a thermal bath in order to perform the tests at body temperature (37 ± 2 °C) and connected to a Gamry Reference 600 Potentiostat/Galvanostat/ZRA. Electrochemical impedance spectroscopy (EIS) measurements were executed after stabilization at open circuit potential (OCP) during 2 h by scanning a range of frequencies from 63 kHz till 10 mHz, with 10 points per frequency decade, with 10 mV amplitude of the sinusoidal signal. Potentiodynamic polarization tests were performed between −0.9 and 1 V_{SCE} with a scanning rate of 1 mV s^{-1}.

3 | RESULTS AND DISCUSSION

Figure 1 presents the dilatometric curves for Ti and Ti–5HAP. Both curves presented very similar behavior until around 860 °C without any significant dimensional changes. Afterwards, the shrinkage rate increased abruptly for Ti, and presented the maximum values between 1080 and 1220 °C.[38] The curve for Ti–5HAP exhibited a significantly different behavior for temperatures above approx. 860 °C. In the literature, different dilatometric curves were reported for HAP compacts. Several authors reported that HAP begins to be sintered at the temperatures between 700 and 800 °C,[41–46]

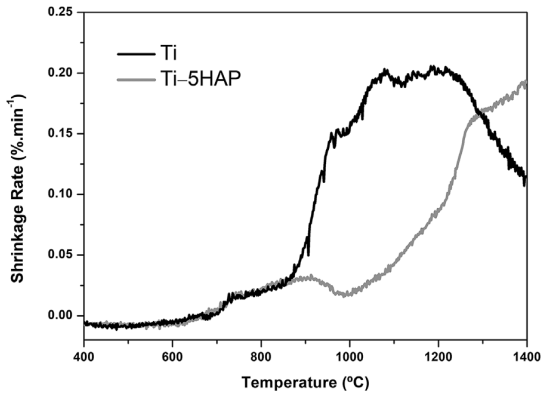

FIGURE 1 Dilatometric curves of Ti[38] and Ti–5HAP

and several sintering temperatures between 1050 and 1250 °C were suggested by combining the dilatometric analysis with other characterization studies.[43–45,47,48] Zhang et al.[45] reported that large shrinkage in the temperature range of 1000–1200 °C corresponds to a higher sintering rate, followed by a soaking period at 1250 °C where densification proceeded with a very slow sintering rate. Therefore, when dilatometric curve of the Ti–5HAP composite (Figure 1) is considered together with the reported results in the literature, it might be suggested that the decrease observed on the shrinkage rate after about 915 °C may be related to the dehydration of HAP.[45] Afterwards, as in accordance with Zhang et al.,[45] large shrinkage was observed between 990 and 1275 °C. After this point, sintering proceeded with a slower rate without presenting any peak on the shrinkage rate until the maximum testing temperature of 1400 °C. However, a noticeable slope was observed on the curve near 1300 °C. Thus, sintering temperature was selected as 1300 °C for the Ti–HAP composites.

Figure 2 presents the low magnification OM images taken from sintered and polished Ti and Ti–5HAP surfaces. Unreinforced Ti samples presented residual porosity (black dots on Figure 2a) typical in conventional powder metallurgy.[38,49] Ti–5HAP composites, on the other hand, presented reasonably homogenous distribution of the HAP particles and/or HAP-depleted zones (dark phases on Figure 2b).

Figure 3 presents higher magnification OM images, as well as SEM images in secondary electron (SE) and backscattered electron (BSE) modes, showing HAP-depleted zones, together with the EDS analysis taken from the HAP-depleted zone. EDS spectrum presents strong peaks of Ti and P, together with weak peaks of Ca. As previously reported in the literature, the HAP-depleted zone may be caused by pulling-out of brittle reaction phases during polishing.[3,14]

Figure 4 represents XRD spectra of raw HAP powders, sintered HAP, and Ti–50HAP composites. Both raw HAP powders and sintered HAP presented only HAP peaks on the spectra (card number of 00-055-0592). Even so, sharper peaks were observed on the sintered powders suggesting that the sample was highly crystalline. Ti–50HAP samples, on the other hand, exhibited the crystal phases of Ti, HAP, TiO, $Ca_4Ti_3O_{10}$, Ti_xPO_y, and P_3Ti_5 (card numbers of 00-044-1294, 00-055-0592, 01-071-5272, 00-014-0152, 01-087-2178, and 00-045-0888, respectively).

Figure 5 shows the representative potentiodynamic polarization curves for the unreinforced Ti and Ti–5HAP composite, and Table 2 presents the corrosion potential ($E_{(i=0)}$) and passivation current density (i_{pass}) values derived from the curves, together with the i_{corr} values obtained by Tafel extrapolation. It can be observed that the unreinforced Ti samples exhibited a well-defined passivation plateau, whereas gradual increases on the anodic current density

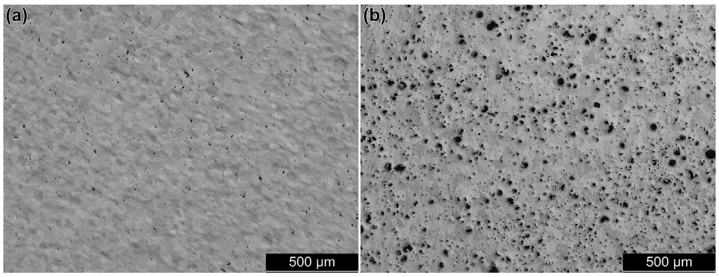

FIGURE 2 Low magnification OM images of a) Ti and b) Ti–5HAP

values were observed on the composite samples at the passive region. This behavior on the composite samples may be attributed to the local active areas formed on the gaps between matrix and the remaining of the ceramic phases, or to the heterogeneities of the oxide film on the HAP-depleted zones. It has been reported for metal matrix composites (MMCs) that discontinuities between matrix and the reinforcement may cause formation of locally activated sites.[50–55] Even so, Ti–5HAP composite samples presented slightly higher $E_{(i=0)}$ values as compared to the unreinforced samples, which can be attributed to the reduced exposed metallic area due to the presence of the ceramic phases, that had also been reported in the literature for several MMCs that can result in a shift on the corrosion potential values to more noble values.[50,52,56–58] In order to have a further understanding of the locally activated sites on the composite samples, EIS studies were performed.

Figure 6 gives the representative EIS spectra in the form of Nyquist and Bode diagrams. Nyquist diagram (Figure 6a) exhibited a smaller diameter of the semi-circle for Ti–5HAP composite samples, as well, Bode diagram presented lower values of $|Z|_{f\to 0}$ as compared to the unreinforced sample, indicating lower corrosion resistance on the composite sample. On the other hand, unreinforced samples presented phase angle values around −83° in low and middle frequency ranges, close to the typical capacitive oxide film formed on the Ti surfaces, whereas the phase angle values were lower for the composites, approaching to maximum values around −72°.

Figure 7 shows the equivalent electrical circuits (EECs) that were used to fit the experimental data for Ti and Ti–5HAP composite. A modified Randle's circuit was used for the unreinforced Ti (Figure 7a) represented by the native oxide film on the surface in contact with the electrolyte, which is the typical EEC used in the literature for commercial pure Ti, composed of R_e (electrolyte resistance), R_{ox} (native oxide film resistance), and Q_{ox} (native oxide film constant phase element, CPE) due to the non-ideal capacitance of the native oxide film. This circuit was not able to represent Ti–5HAP composite, thus, the EEC shown in Figure 7b was used for the composite, containing additional circuit elements representing the electrochemical activity taking place in the HAP-depleted zones, namely R'_e, representing an additional electrolyte resistance, R_{ct}, representing the charge transfer resistance, and $Q_{dl,}$ representing the non-ideal capacitance of the electric double layer. R_{ox} is removed from the EEC since it tended to be extremely high thus not allowing conduction of electrons.[51]

The fitting was performed using Gamry Echem Analyst software (version 5.61) where CPE was used for allowing the deviation of ideal behavior of a capacitor. The impedance of CPE is defined as in Eq. (1):

$$Z_{CPE} = \frac{1}{Y_0(jw)^n} \tag{1}$$

where Y_0 is a frequency-independent constant, $j = (-1)^{1/2}$, w is the angular frequency, and n is the fractional exponent representing irregularities of the surface.[59–61] When $n = 1$, the response of CPE corresponds to a capacitor whereas when $n \approx 1$, CPE is considered as a non-ideal capacitor, where n values are affected by surface roughness and heterogeneities.

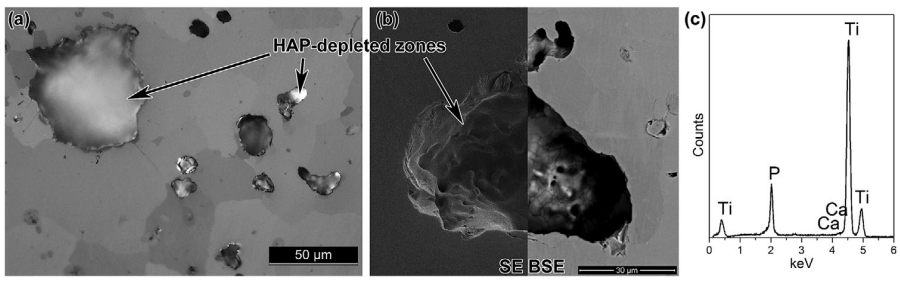

FIGURE 3 a) OM and b) SEM image of the Ti–5HAP composite; c) EDS spectrum taken from the HAP-depleted zone presented on (b)

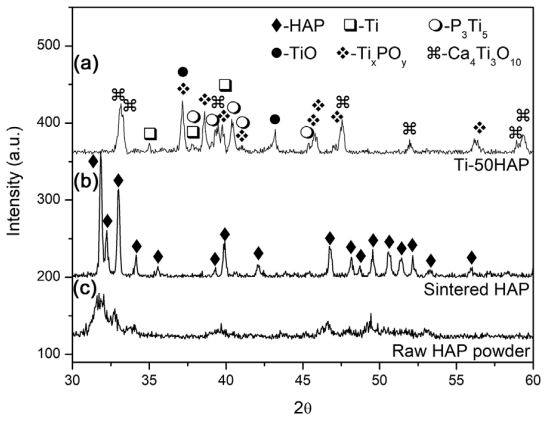

FIGURE 4 XRD spectra of a) raw and b) sintered HAP powders, together with c) Ti–50HAP composites

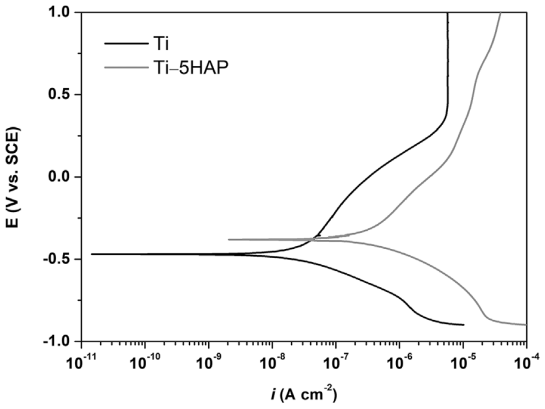

FIGURE 5 Representative potentiodynamic polarization curves for Ti and Ti–5HAP composite samples in 0.9 wt% NaCl

The proposed models assumed to describe adequately the behavior of the unreinforced Ti and Ti–5HAP composite since the goodness of fitting were below 10^{-4}. Table 3 presents the EEC parameters obtained from EIS data where Q values were converted to C (capacitance) by using Eqs. (2) and (3) derived from Brugg's equation.[62]

$$C_{ox} = \left[Q_{ox} R_e^{(1-n)}\right]^{\frac{1}{n}} \quad (2)$$

$$C_{dl} = \left[Q_{dl}(R_e + R_e'^{(1-n)})\right]^{\frac{1}{n}} \quad (3)$$

C_{ox} values obtained from Ti–5HAP samples presented clearly higher average values suggesting lower quality of the native oxide film formed on Ti–5HAP sample surfaces in contact with the electrolyte. Besides, lower n_{ox} values obtained from Ti–5HAP samples pointed to heterogeneities on their surfaces. As it was discussed above, within the testing temperature range, the dilatometric curve of Ti–5HAP did not present a peak pointing to the maximum shrinkage rate. Thus, apparently the addition of HAP particles, and their decomposition during processing changed the sintering kinetics, which may create differences on the matrix surfaces, such as uncompleted sintering, and therefore, may affect the properties of the native oxide film formed on the matrix surfaces. Nevertheless, the biggest difference on the electrochemical response between Ti and Ti–5HAP samples was caused by the HAP-depleted zones on the composite. First, the pores formed after HAP decomposition led to obtain an additional electrolyte resistance on these zones.[51,52] More importantly, as represented on the EEC (Figure 7b) by the R_{ct}/Q_{dl} couple, local active areas were characterized on the HAP-depleted zones. Although n_{dl} presented lower values as compared to n_{ox} values obtained from both samples, indicating more heterogeneous surfaces on the HAP-depleted zones, C_{dl} and R_{ct} values were close to C_{ox} and R_{ox} values of Ti samples, respectively. Therefore, although a dense and compact film was not formed on the metallic surfaces between the HAP remnants or decomposition products (Figure 7), apparently, these sites contributed to the overall corrosion resistance.[63]

When immersed to electrolytes containing organic ions, Ti is able to naturally form calcium phosphates on its passive film. Hanawa and Ota[64] reported that the calcium phosphate can exist on the surface as islands deposited on the titanium oxide. Accordingly, it may be speculated that the electrochemical activity found on the HAP-depleted zones may be related to such a heterogeneous film also often disturbed by the ceramic phases of HAP remnants or HAP decomposition products. However, it is clear that further characterization studies of these zones need to be done by transmission electron microscopy (TEM) and X-ray photoelectron spectroscopy (XPS). Furthermore, ion releasing on the HAP-depleted zones should be quantified and biological response of these surfaces should be studied. On the other hand, one of the certain limitations of the present work was to perform XRD analysis on the Ti–50HAP samples (in order to have a better quantification of the decomposition phases), whereas electrochemical studies were performed on the Ti–5HAP

TABLE 2 Electrochemical values obtained from potentiodynamic polarization curves

Samples	$E_{(i=0)}$ (mV vs. SCE)	i_{corr} (μA cm^{-2})	i_{pass} (μA cm^{-2})
Ti	−428 ± 81	–	5.75 ± 0.70
Ti–5HAP	−377 ± 32	0.15 ± 0.03	–

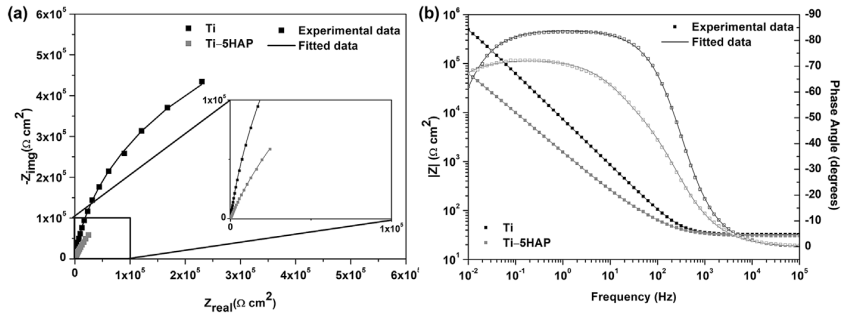

FIGURE 6 EIS spectra in the form of a) Nyquist and b) Bode diagrams of experimental data and fitted curves for Ti and Ti–5HAP in 0.9 wt% NaCl

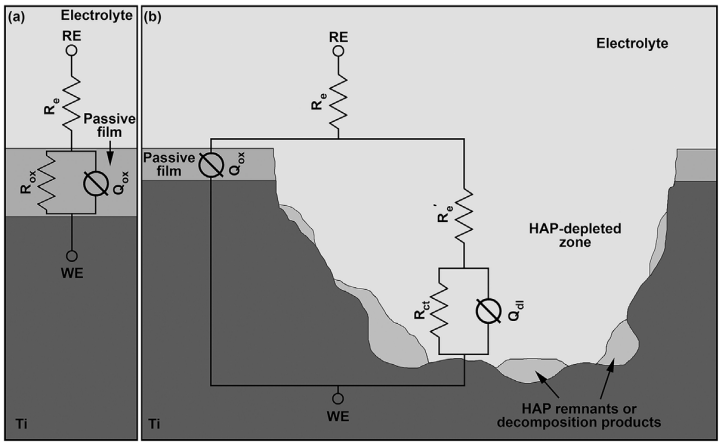

FIGURE 7 EECs used for fitting the experimental data for a) Ti, and b) Ti–5HAP

TABLE 3 EEC parameters obtained from EIS data

Samples	C_{ox} (μF cm^{-2})	n_{ox}	R_{ox} (KΩ cm^2)	C_{dl} (μF cm^{-2})	n_{dl}	R_{ct} (MΩ cm^2)
Ti	15 ± 4	0.93 ± 0.01	1.11 ± 0.22	–	–	–
Ti–5HAP	93 ± 45	0.88 ± 0.06	–	8 ± 3	0.78 ± 0.08	1.06 ± 0.31

samples. Thus, HAP decomposition and its influence on the electrochemical and biological properties should be studied as a function of the reinforcement volume fraction. Finally, since these surfaces can be a candidate for load-bearing dental and orthopaedic applications, tribocorrosion behavior should also be evaluated.

4 | CONCLUSIONS

Within the framework of this study, it can be concluded that the decomposition of HAP led to the formation of HAP-depleted zones having discontinuous ceramic phases containing Ca and P. These zones resulted in an inferior corrosion behavior evidenced by gradual increases of the current density values on the passive zone of the polarization curves. Further electrochemical analyses by EIS showed lower |Z| values for the composite samples and revealed a local electrochemical activity on the HAP-depleted zones by a presence of an additional electrolyte resistance, charge transfer resistance, and non-ideal capacitance of the double-layer.

ACKNOWLEDGMENTS

This study was supported by the Foundation for Science and Technology (FCT), Portugal with the reference projects UID/EEA/04436/2013, EXCL/SEM-TEC/0460/2012, and M-ERA-NET/0001/2015, as well, by FEDER funds through the

COMPETE 2020 – Programa Operacional Competitividade e Internacionalização (POCI) with the reference project POCI-01-0145-FEDER-006941. The authors would also like to acknowledge Prof. Ana Senos (University of Aveiro) and Prof. José Carlos Teixeira (University of Minho) for the provision of the characterization facilities.

ORCID

Fatih Toptan http://orcid.org/0000-0001-9138-9119

REFERENCES

[1] C. Q. Ning, Y. Zhou, *Biomaterials* **2004**, *25*, 3379.
[2] W. Shi, A. Kamiya, J. Zhu, A. Watazu, *Mater. Sci. Eng. A* **2002**, *337*, 104.
[3] Anawati, H. Tanigawa, H. Asoh, T. Ohno, M. Kubota, S. Ono, *Corros. Sci*. **2013**, *70*, 212.
[4] X. Zhou, P. Mohanty, *Electrochim. Acta* **2012**, *65*, 134.
[5] S. B. Goodman, Z. Yao, M. Keeney, F. Yang, *Biomaterials* **2013**, *34*, 3174.
[6] C. Q. Ning, Y. Zhou, *Biomaterials* **2002**, *23*, 2909.
[7] L. Zhang, Z. Y. He, Y. Q. Zhang, Y. H. Jiang, R. Zhou, *Mater. Sci. Eng. C* **2016**, *67*, 104.
[8] A. Kumar, K. Biswas, B. Basu, *J. Biomed. Mater. Res. Part A* **2015**, *103*, 791.
[9] K. Niespodziana, K. Jurczyk, J. Jakubowicz, M. Jurczyk, *Mater. Chem. Phys*. **2010**, *123*, 160.
[10] H. Ye, X. Y. Liu, H. Hong, *J. Mater. Sci. Mater. Med*. **2009**, *20*, 843.
[11] Q. Chang, D. L. Chen, H. Q. Ru, X. Y. Yue, L. Yu, C. P. Zhang, *Biomaterials* **2010**, *31*, 1493.
[12] S. Salman, O. Gunduz, S. Yilmaz, M. L. Oveçoglu, R. L. Snyder, S. Agathopoulos, F. N. Oktar, *Ceram. Int*. **2009**, *35*, 2965.
[13] C. Ning, Y. Zhou, *Acta Biomater*. **2008**, *4*, 1944.
[14] P. Balbinotti, E. Gemelli, G. Buerger, S. A. de Lima, J. de Jesus, N. H. A. Camargo, V. A. R. Henriques, G. D. A. de Soares, *Mater. Res*. **2011**, *14*, 384.
[15] A. Kumar, K. Biswas, B. Basu, *J. Phys. D-Appl. Phys*. **2013**, *46*, 404004.
[16] D. Bovand, M. Yousefpour, S. Rasouli, S. Bagherifard, N. Bovand, A. Tamayol, *Mater. Des*. **2015**, *65*, 447.
[17] A. Fahami, R. Ebrahimi-Kahrizsangi, B. Nasiri-Tabrizi, *Solid State Sci*. **2011**, *13*, 135.
[18] T. M. Marcelo, V. Livramento, M. V. de Oliveira, M. H. Carvalho, *Mater. Res*. **2006**, *9*, 65.
[19] F. Watari, A. Yokoyama, M. Omori, T. Hirai, H. Kondo, M. Uo, T. Kawasaki, *Compos. Sci. Technol*. **2004**, *64*, 893.
[20] C. Popa, V. Simon, I. Vida-Simiti, G. Batin, V. Candea, S. Simon, *J. Mater. Sci. Mater. Med*. **2005**, *16*, 1165.
[21] C. Chenglin, Z. Jingchuan, Y. Zhongda, W. Shidong, *Mater. Sci. Eng. A* **1999**, *271*, 95.
[22] X. Zheng, M. Huang, C. Ding, *Biomaterials* **2000**, *21*, 841.
[23] S. J. Ding, *Biomaterials* **2003**, *24*, 4233.
[24] H. Ye, X. Y. Liu, H. Hong, *Mater. Sci. Eng. C* **2009**, *29*.
[25] Y. W. Gu, K. A. Khor, P. Cheang, *Biomaterials* **2003**, *24*, 1603.
[26] C. Chen, T. Huang, C. Kao, S. Ding, *J. Biomed. Mater. Res. Part B Appl. Biomater*. **2005**, *77*, 146.
[27] K. Ozeki, T. Yuhta, Y. Fukui, H. Aoki, I. Nishimura, *J. Mater. Sci. Mater. Med*. **2002**, *13*, 253.
[28] M. Inagaki, Y. Yokogawa, T. Kameyama, *J. Mater. Sci. Mater. Med*. **2003**, *14*, 919.
[29] W.-G. Kim, H.-C. Choe, *Thin Solid Films* **2011**, *519*, 7045.
[30] X. F. Xiao, R. F. Liu, Y. Z. Zheng, *Mater. Lett*. **2005**, *59*, 1660.
[31] M. R. Mansur, J. Wang, C. C. Berndt, *Surf. Coatings Technol*. **2013**, *232*, 482.
[32] J. Cihlár, A. Buchal, M. Trunec, *J. Mater. Sci*. **1999**, *34*, 6121.
[33] T. Wang, A. Dorner-Reisel, E. Müller, *J. Eur. Ceram. Soc*. **2004**, *24*, 693.
[34] C. J. Liao, F. H. Lin, K. S. Chen, J. S. Sun, *Biomaterials* **1999**, *20*, 1807.
[35] A. Arifin, A. B. Sulong, N. Muhamad, J. Syarif, M. I. Ramli, *Mater. Des*. **2014**, *55*, 165.
[36] J. Weng, X. Liu, X. Zhang, X. Ji, *J. Mater. Sci. Lett*. **1994**, *13*, 159.
[37] Y. Yang, K. H. Kim, C. M. Agrawal, J. L. Ong, *Biomaterials* **2004**, *25*, 2927.
[38] A. C. Alves, I. Sendão, E. Ariza, F. Toptan, P. Ponthiaux, A. M. P. Pinto, *J. Porous Mater*. **2016**, *23*, 1261.
[39] H. Matusiewicz, *Acta Biomater*. **2014**, *10*, 2379.
[40] A. Balamurugan, S. Rajeswari, G. Balossier, A. H. S. Rebelo, J. M. F. Ferreira, *Mater. Corros*. **2008**, *59*, 855.
[41] T. V. Safronova, V. I. Putlyaev, M. A. Shekhirev, Y. D. Tretyakov, A. V. Kuznetsov, A. V. Belyakov, *J. Eur. Ceram. Soc*. **2009**, *29*, 1925.
[42] G. Carotenuto, G. Spagnuolo, L. Ambrosio, L. Nicolais, *J. Mater. Sci. Mater. Med*. **1999**, *10*, 671.
[43] E. Saiz, L. Gremillard, G. Menendez, P. Miranda, K. Gryn, A. P. Tomsia, *Mater. Sci. Eng. C* **2007**, *27*, 546.
[44] A. Bianco, I. Cacciotti, M. Lombardi, L. Montanaro, *Mater. Res. Bull*. **2009**, *44*, 345.
[45] X. Zhang, G. H. M. Gubbels, R. A. Terpstra, R. Metselaar, *J. Mater. Sci*. **1997**, *32*, 235.
[46] D. Bernache-Assollant, A. Ababou, E. Champion, M. Heughebaert, *J. Eur. Ceram. Soc*. **2003**, *23*, 229.
[47] G. Bezzi, G. Celotti, E. Landi, T. M. G. La Torretta, I. Sopyan, A. Tampieri, *Mater. Chem. Phys*. **2003**, *78*, 816.
[48] T. V. Safronova, M. A. Shekhirev, V. I. Putlyaev, *Glas. Ceram. (English Transl. Steklo i Keramika)* **2007**, *64*, 408.
[49] H. L. Bi, C. Z. Yu, P. Cao, Y. H. He, *Key Eng. Mater*. **2012**, *520*, 76.
[50] Z. Doni, A. C. Alves, F. Toptan, A. M. Pinto, L. A. Rocha, M. Buciumeanu, L. Palaghian, F. S. Silva, *Tribol. – Mater. Surf. Interfaces* **2014**, *8*, 201.
[51] A. M. Ribeiro, A. C. Alves, F. S. Silva, F. Toptan, *Mater. Corros*. **2015**, *66*, 790.
[52] F. Toptan, A. Rego, A. C. Alves, A. Guedes, *J. Mech. Behav. Biomed. Mater*. **2016**, *61*, 152.
[53] D. J. Lloyd, *Int. Mater. Rev*. **1994**, *39*, 1.
[54] P. P. Trzaskoma, E. McCafferty, C. R. Crowe, *J. Electrochem. Soc*. **1983**, *130*, 1804.
[55] Z. Oksiuta, J. R. Dabrowski, A. Olszyna, *J. Mater. Process. Technol*. **2009**, *209*, 978.
[56] I. Garcia, A. Conde, G. Langelaan, J. Fransaer, J. P. Celis, *Corros. Sci*. **2003**, *45*, 1173.
[57] T. Lampke, A. Leopold, D. Dietrich, G. Alisch, B. Wielage, *Surf. Coatings Technol*. **2006**, *201*, 3510.

[58] A. M. Ribeiro, A. C. Alves, L. A. Rocha, F. S. Silva, F. Toptan, *Tribol. Int*. **2015**, *91*, 198.
[59] N. Figueira, T. M. Silva, M. J. Carmezim, J. C. S. Fernandes, *Electrochim. Acta* **2009**, *54*, 921.
[60] Y. Dai, Q. Li, H. Gao, L. Q. Li, F. N. Chen, F. Luo, S. Y. Zhang, *Surf. Eng*. **2011**, *27*, 536.
[61] G. Gao, C. Liang, *Electrochim. Acta* **2007**, *52*, 4554.
[62] M. E. Orazem, B. Tribollet, *Electrochemical Impedance Spectroscopy*, Jonh Wiley & Sons, New Jersey **2008**.
[63] N. D. Nam, M. J. Kim, D. S. Jo, J. G. Kim, D. H. Yoon, *Thin Solid Films* **2013**, *545*, 380.
[64] T. Hanawa, M. Ota, *Appl. Surf. Sci*. **1992**, *55*, 269.

How to cite this article: Toptan F, Alves AC, Ferreira MA, da Silva Oliveira CI, Pinto AM. Effect of HAP decomposition on the corrosion behavior of Ti–HAP biocomposites. *Materials and Corrosion*. 2018;69: 1292–1299. https://doi.org/10.1002/maco.201810049